3D Printed Templating of Extrinsic Freeze-Casting for Macro–Microporous Biomaterials

Jae-Young Jung,[†,‡] Steven E. Naleway,[†,§] Yajur N. Maker,[⊥] Kathryn Y. Kang,[⊥] Jaehong Lee,[∥,#] Jungmin Ha,[‡] Sung Sik Hur,[*,⊥,∥] Shu Chien,[⊥,∥] and Joanna McKittrick[‡,∇]

‡Materials Science and Engineering Program, ⊥Department of Bioengineering, ∥Institute of Engineering in Medicine, #Department of Biological Sciences, and ∇Department of Mechanical and Aerospace Engineering, University of California San Diego, La Jolla, California 92093, United States

§Department of Mechanical Engineering, The University of Utah, Salt Lake, Utah 84112, United States

S *Supporting Information*

ABSTRACT: As with most biological materials, natural bone has hierarchical structure. The microstructural features of compact bone are of various length scales with its porosity consisting of larger osteons (∼100 μm diameter) and vascular channels, as well as smaller lacuna spaces (∼10 μm diameter). In this study, the freeze-casting process, which has been previously used to form biocompatible porous scaffolds (made with hydroxyapatite, HA) has been improved to mimic the intrinsic hierarchical structure of natural bone by implementing an extrinsic 3D printed template. The results of pore characterization showed that this novel combined method of 3D printing and freeze-casting is able to produce porosity at multiple length scales. Nonporous, microporous (created with freeze-casting alone), and macro-micro porous (created with freeze-casting and 3D printed templating) scaffolds were compared as substrates to evaluate cellular activities using osteoblast-like MG63 cell lines. The number of cells oriented parallel to the HA wall structures in the freeze-cast scaffold was found to increase on the microporous and macro-micro porous samples when compare to the nonporous samples, mimicking the natural alignment of the lamella of natural bone. Regarding the cell morphologies, cells on microporous and macro-micro porous samples showed narrowly aligned shapes, whereas those on nonporous samples had polygonal shapes with no discernible orientation. Proliferation and differentiation tests demonstrated that no toxicity or functional abnormalities were found in any of the substrates due to potential chemical and mechanical residues that may have been introduced by the freeze-casting process. Monitoring of the three-dimensional distribution of cells in the scaffolds through microcomputed tomography indicates that the cells were well distributed in the interior pore spaces via the interpenetrating macro-micro pore networks. In summary, we demonstrate this novel approach can create porosity at multiple length scales and is highly favorable in creating a biocompatible, osteoconductive, and structurally hierarchical HA scaffolds for biomedical applications.

KEYWORDS: *freeze-casting, 3D printing, macro-micro porous scaffold, pore shape and size control, osteoblast-like MG63 cell lines, biomedical implant materials*
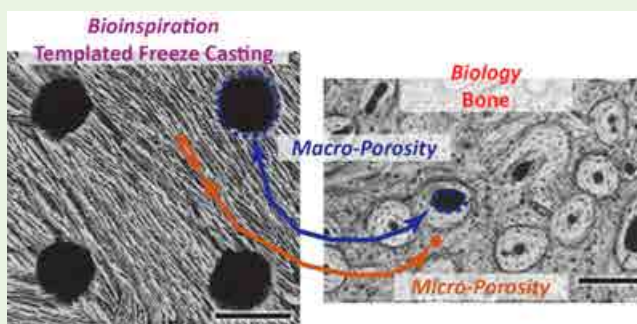
1. INTRODUCTION

The bioinspiration process takes guidance from the successful strategies of natural and biological materials and harnesses them to develop novel materials that can provide benefits to society. This bioinspiration process does not necessarily look to mimic nature in its entirety but merely to employ its most important elements. When considering the structure and properties of biological materials there are a number of qualities that set them apart from synthetics.[1−3] Perhaps one of the most important characteristics is their hierarchical structuring at multiple length scales, which allows for all types of outstanding properties from the impact-resistant dactyl clubs of the mantis shrimp[4] to the remarkable toughness of abalone nacre.[5,6] In many ways, this hierarchical structuring is the result of the common theme of

templating within biological materials, where a biopolymer (e.g., collagen) provides a template for the nucleation and growth of a biomineral (e.g., hydroxyapatite, HA).[7] This hierarchical structuring, and the beneficial properties that it provides, is a desired quality when these natural structures are converted into bioinspired designs.

One such avenue of bioinspired design comes from the freeze-casting processing method. In general, this method is carried out in four distinct steps: (1) a liquid slurry consisting of solid loading particles and a liquid freezing agent is mixed, (2)

this slurry is directionally frozen so that the freezing agent is able to template the ceramic particles as it solidifies, (3) the frozen freezing agent is sublimed out to create a green scaffold, (4) the green scaffold is sintered to form a final, aligned porous scaffold.[8−11] The most important step is (2), where the scaffold is templated through directional freezing to mimic the natural templating found within biological materials. In spite of this connection, the structures created by freeze-casting are often confined to a single length scale and constrained by the rate and direction of the freezing front. This prevents the formation of multidimensional structures with varying porosities and mechanical properties that replicate the unique advantages created naturally in biological tissues and materials. While there have been a number of reports of methodologies to create gradients in the microstructural pore size through freeze-casting,[12−15] the creation of freeze-cast scaffolds with inter-penetrating porosity at multiple length scales has proven difficult to achieve.

Freeze-casting has been suggested a number of times for the fabrication of bioinspired bone.[12,16−19] This is largely due to the processes' ability to mimic the material constituents and, to some extent, the porous structure of natural bone. However, the porosity in bone occurs at multiple length scales, with larger osteons and vascular channels (occurring on the length scale of ~100 μm) and smaller lacuna spaces (occurring on the length scale of ~10 μm).[20] Although the freeze-casting technique has been able to produce a variety of complex porous micro-structures, to the best of the authors' knowledge, these structures have never been demonstrated at multiple length scales within a single material.

We propose a novel freeze-casting method for the creation of bioinspired materials that exhibit porosity at multiple length scales through the use of a 3D printed template (creating "macroporosity") to supplement the templating of growing ice crystals that are integral to freeze-casting (to create "micro-porosity"). To evaluate the effect of this porosity at multiple length scales on cellular activity and biocompatibility, we cultured osteoblast-like MG63 cells to demonstrate cell morphology, alignment, and the number of cells attached before the doubling time. In addition, cell proliferation and differentiation were evaluated to assess the toxicity, or lack thereof, of the residual materials from the freeze-casting process and essential cellular functions, respectively. Through this study, scaffolds inspired by natural compact bone are shown to be a viable candidate for an osteoconductive cell culture substrate for future orthopedic applications.

2. MATERIALS AND METHODS

2.1. Sample Preparation. To compare the effects of cell growth due to macro- or microporosity, three types of samples were prepared with the same HA material constituent: nonporous (flattened, polished surface as a negative control), microporous only, and macro-micro porous samples (Figure 1). Of note, because of the sintering processes involved with each sample fabrication technique, all of the final samples were made of pure HA. The definition of the porosity size is given as macroporous (>100 μm) and microporous (<20 μm).[21]

All samples fabricated in this research were made from the same base constituent of HA powder (200−500 nm in diameter, Trans-Tech, Adamstown, MA, USA). This was mixed with poly(vinyl alcohol) (PVA, Alfa Aesar, Ward Hill, MA, USA) and polyethylene glycol (PEG, Alfa Aesar, Ward Hill, MA, USA) to function as organic binders and facilitate the fabrication processes. A dispersant (Darvan 811, an ammonium polymethacrylate anionic dispersant, R. T.
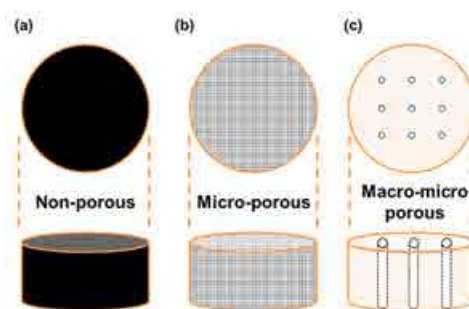
Figure 1. Schematic diagrams of sample porosity: (a) Nonporous: 99 wt % HA, these samples serve as a negative control to test the effect of pores on cellular activities. (b) Micropore only (~20 μm): 20 vol % HA, freeze-casted using conventional methods.[18,22] (c) Macro−micro ore: macro-ores incorporated through adapting conventional freeze-casting methods with 3D printed templates, thus forming pores at two length scales (~20 μm and 600−800 μm for micro- and macropores, respectively).

Vanderbilt Company, Inc., Norwalk, CT, USA) was used to ensure an even distribution of the HA powers and organic binders.

2.1.1. Nonporous (NP) Sample. 99 wt % HA powder was mixed with 1 wt % PVA with a molecular weight of 100 000 g/mol. The mixture was poured into individual containers to form discs that were approximately 20 mm in diameter and 7 mm in height. These individual samples were sintered in an open-air furnace for 3 h at 1623 K with heating and cooling rates of 2 K/min. This sintering procedure is similar to previously reported procedures for HA freeze cast scaffolds.[18,22] After sintering, each sample was polished on all surfaces using P600 and P1200 silicon carbide sandpaper (Buehler, Lake Bluff, IL, USA), sequentially, to form a final smooth, flattened surface. The dimension of each final sample was 17 mm in diameter and 5 mm in height.

2.1.2. Microporous (μP) Sample. Conventional freeze-casting methods were used to prepare the microporous samples. Aqueous slurries consisting of 20 vol % HA powder were mixed with 1 wt % PEG with a molecular weight of 10 000 g/mol and 1 wt % PVA with a molecular weight of 100 000 g/mol, and 1 wt % of Darvan 811. These slurries were ball-milled in an alumina grinding media for 24 h then degassed under low vacuum for 5−10 min. Samples of ~10 mL of the degassed slurry were poured into a freeze-cast mold ~20 mm in diameter and 50 mm in height. Samples were then frozen at a constant rate of 10 K/min using a custom built freeze-casting device, as previously described.[23] After freezing, samples were freeze-dried in a benchtop freeze-dryer (Labconco, Kansas City, MO, USA) at 223 K and 350 Pa for 70 h. After freeze-drying, the green scaffolds were sintered in an open-air furnace for 3 h at 1623 K with heating and cooling rates of 2 K/min. After sintering, the samples were wrapped in 200 μm thick polylactic acid (PLA) shrink-wrap (WestRock, Croydon, PA, USA) using a spray adhesive (3M, St. Paul, MN, USA). The samples were placed in a 373 K oven for 10 min to induce shrinkage of the PLA film and create a compact scaffold that could easily be manipulated for cutting. To avoid edge effects during fabrication, 10 mm of material was cut off of each end of the scaffolds using a laboratory sectioning saw (MARK V LAB, East Granby, CT, USA). Each scaffold was then cut into three 7 mm thick discs and each disc was sanded down on top and bottom surfaces using the previously described method for nonporous scaffolds to create the final microporous samples approximately 17 mm in diameter and 5 mm in height.

2.1.3. Macro- and microporous (mP) Sample and Pore Size Control by Templates. To induce macro-porosity in freeze-cast scaffolds, templates were 3D printed using a ProJet 3510 HD printer (3D Systems, Rock Hill, SC, USA) and were fabricated out of a ProJet VisiJet M3-X polymer (similar in properties to extruded acrylonitrile butadiene styrene plastic[24]). These templates were designed with an array of high-aspect ratio pins as well as a support structure (solid

models are shown in Figure 2). This support structure consists of longitudinal beams and transverse brackets, which were necessary to
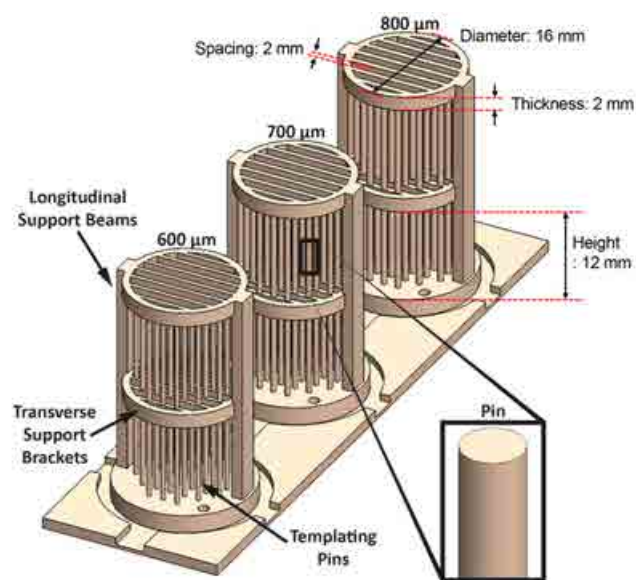
Figure 2. Solid models of the 3D printed templates, highlighting the templating pins, longitudinal support beams, and transverse support brackets. Templates with 600 μm, 700 and 800 μm diameter pins were connected with sacrificial material so as to be printed together. The inset shows the circular cross-section of each of the pins. The diameter, thickness, and the height of the transverse support brackets are 16, 2, and 12 mm, respectively.

ensure the stability of the pins during the printing and freezing processes. Templates were created with pins of a round cross-section and diameters of 600, 700, and 800 μm. The spacing between pins was 2 mm. Templates were printed together, connected with a sacrificial material, so as to limit manufacturing time. To prepare the macro–microporous samples, a similar procedure to preparing the microporous samples using conventional freeze-casting was followed.

The same slurry described above was prepared and poured into the same freeze-casting mold. Prior to the freezing step, a 3D printed template was suspended upside down in the slurry, as shown in Figure 3. The sample was similarly freeze-dried and sintered using the same sintering profile as described above. During this sintering process, the 3D printed template was completely burned out, leaving in its wake macro-porosity. Similar to the microporous samples, these 3D templated samples were wrapped in the 200 μm thick PLA shrink-wrap and placed in a 373 K oven for 10 min to induce shrinkage of the film. Five mm of material was removed from both ends of each scaffold and then the scaffold was cut into two discs, which were each 7 mm in height, and sanded down on top and bottom surfaces using the previously described method for nonporous scaffolds to form the final macro–microporous samples that were each ∼17 mm in diameter and 5 mm in height. A total of 18 nonporous, 18 microporous, and 18 macro-micro porous samples were created.

2.2. Material Characterization. All scaffolds were observed with scanning electron microscopy (SEM) at 10 kV and a spot size of 3 nm using a field-emission environmental SEM (Philips XL30, FEI Company, Hillsboro, OR, USA). For SEM preparation, transverse cross sections, approximately 5 mm from the top surface of the scaffolds, were sectioned and polished with fine grit sand paper. All samples were sputter-coated with iridium using an Emitech K575X sputter coater (Quorum Technologies Ltd., West Sussex, UK). Microstructural measurements of the pore size were performed using ImageJ software (National Institutes of Health, Bethesda, MD, USA). To calculate the mean and standard deviation, $N = 40$ measurements of micropores and $N = 20$ measurements of macropores were taken for three scaffolds each of the macro-microporous scaffolds with pins of
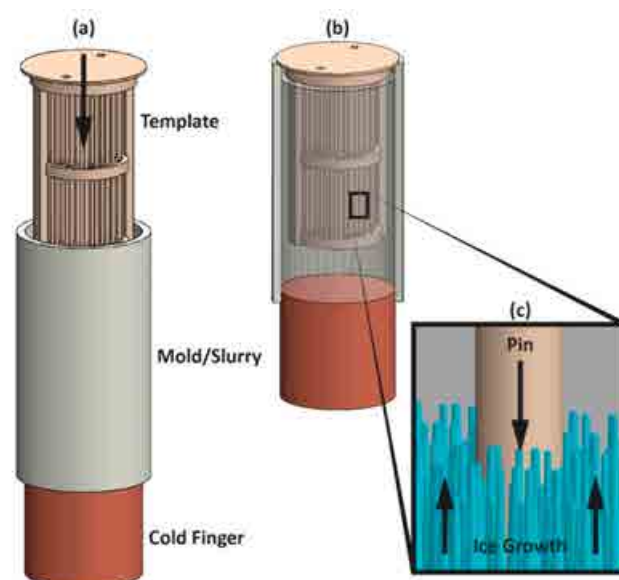
Figure 3. Methodology for templated freeze-casting. (a) 3D printed template is placed within a mold and immersed in slurry, which is affixed on top of a coldfinger to provide directional freezing; (b) The template is suspended above the coldfinger but fully immersed in the slurry; (c) During freezing, the template deflects ice growth, allowing for two length scales of porosity after sintering.

600, 700, and 800 μm, respectively. Measurements of macro-porosity were limited due to the total number of pores in each scaffold. Measurements of pore size and shape for all pores were performed by using an ImageJ software, adjusting the threshold of the micrographs (using a consistent threshold for all measurements) so as to fit an ellipse to the pores to determine the elliptic major axis, a, and minor axis, b. The assumption of elliptical pores has been previously employed for freeze-cast scaffolds with similar architecture[22,25−27] and was supported through observations of the pore shape within the current scaffolds. Pore area, A_p, and pore aspect ratio, X_p, were calculated as $A_p = ab\pi/4$ and $X_p = a/b$, respectively. In addition, for each macro-pore, a characteristic diameter, D_{eff}, was calculated as $D_{eff} = (a + b)/2$. Relative densities of materials were calculated as a fraction of materials for each sample multiplied the bulk density of hydroxyapatite (2.6 g/cm³[28]). An X-ray Diffraction (XRD) analysis was performed with the ground powders of an mP sample at 30 kV with 10 mA (D2 Phaser, Bruker, Karlsruhe, Germany) using CuKα radiation and a step size of 0.014° over a 2θ range of 20 to 80°.

2.3. Cell Culture. For cell culture tests, samples with three distinct conditions were tested: nonporous samples (NP), microporous samples (μP), and macro-micro porous samples (mP) (with 600 μm macropores with 4 mm spacing between two longitudinal pins). The scaffolds with a 600 μm of diameter was chosen for cell culture tests for two main reasons: First, it had the largest surface area of the solid substrates where the cells can attach, proliferate, and differentiate to show their basic biological function and viability. Second, the 600 μm samples had the highest mechanical stability due to the relatively larger proportion of dense material when compared to the scaffolds with other pore sizes (700 and 800 μm) as shown by the results on the bulk density of the scaffolds in Table 1.

2.3.1. Cell Culture and Seeding for 3D HA Scaffold. The biological activities of osteoblast-like MG63 human cell lines (MG63s) on the fabricated scaffolds were evaluated by adhesion, proliferation, and differentiation tests. MG63s were seeded onto the three kinds of specimens: NP, μP, and mP. The cell densities were varied along three tests, as described in the preceding sections. The cells were cultured in a 10 cm Petri dish containing Dulbecco's modified Eagle's medium (DMEM) supplemented with 10% fetal bovine serum (FBS), 1% sodium pyruvate, 1% L-glutamine, and 1% penicillin-streptomycin. Cells were maintained in an incubator with 5% CO_2 and 95%

Table 1. Pore Measurements for Both Micro- And Macroporosity[a]

		control	600 μm	700 μm	800 μm
microporosity	a (μm)	124.9 ± 38.7	135.2 ± 42.1	144.0 ± 44.9	118.5 ± 37.9
	b (μm)	20.5 ± 4.4	21.8 ± 5.0	19.3 ± 4.2	23.6 ± 8.0
	A_p (μm^2)	2,058 ± 903	2,354 ± 960	2,211 ± 973	2,266 ± 1,208
	X_p	6.24 ± 1.90	6.39 ± 2.14	7.72 ± 2.46	5.38 ± 2.00
macroporosity	a (μm)		585.6 ± 36.5	688.8 ± 29.8	748.5 ± 30.6
	b (μm)		512.1 ± 30.8	573.4 ± 32.5	659.7 ± 34.9
	A_p (μm^2)		235,551 ± 20,161	310,476 ± 26,200	387,695 ± 23,947
	X_p		1.15 ± 0.10	1.20 ± 0.07	1.14 ± 0.08
	D_{eff} (μm)		548.9 ± 23.8	631.1 ± 26.1	704.1 ± 21.4
percentage of hydroxyapatite in scaffold (%)		53.54 ± 3.2	48.31 ± 0.6	45.69 ± 4.6	39.19 ± 3.3
bulk density of scaffold (g/cm^3)		1.39 ± 0.08	1.27 ± 0.02	1.19 ± 0.12	1.02 ± 0.09

[a]Results are shown as the average ± standard deviation for 40 measured pores in the case of microporosity and 20 measured pores in the case of macroporosity. a, the elliptic major axis; b, minor axis; A_p, pore area (=$ab\pi/4$), X_p, a/b; and D_{eff}, a characteristic dimension (= $(a + b)/2$). Relative densities of the scaffolds are calculated as the fraction of materials for each sample multiplied by the bulk density of hydroxyapatite (2.6 g/cm^3).[28]
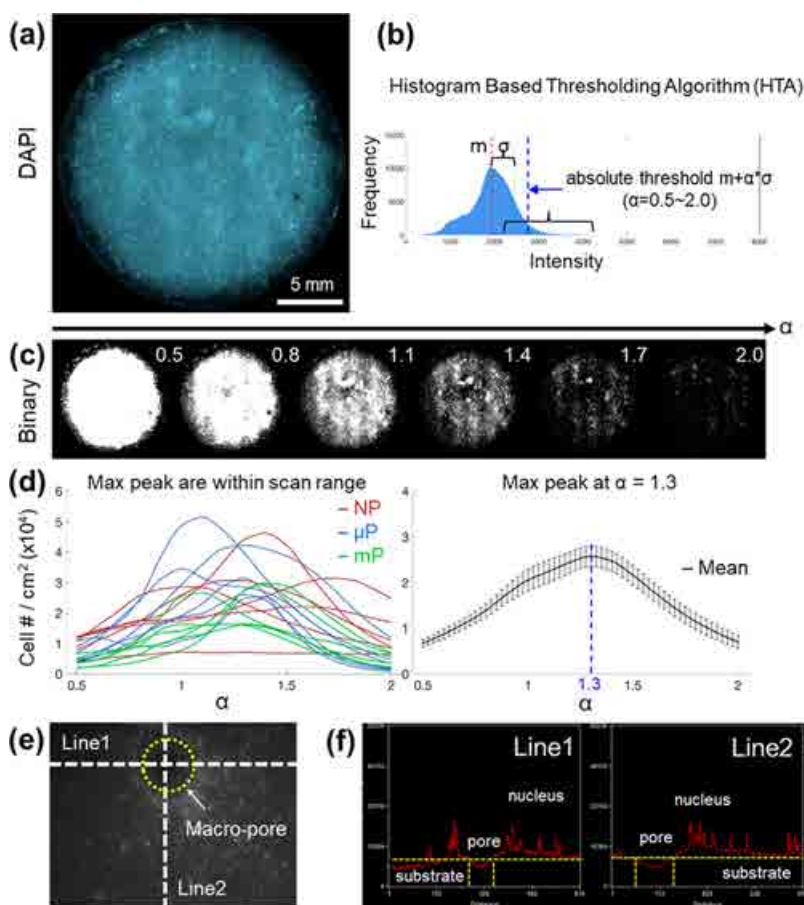
Figure 4. Measurement of nuclei number using histogram-based thresholding. (a) DAPI image of a whole HA sample (NP). 80 planes (10 sets of 8 images) of 4× images are stitched together (a total of 5670 × 5272 pixels in the image, 960 × 720 pixels/image) to form this image. Pixels outside of the sample are removed to eliminate background pixels from the histogram. (b) An intensity histogram of the image in panel a. The threshold value is determined from the mean (m) and the standard deviation (σ), i.e., the threshold value = $m + \alpha*\sigma$. α is a multiplier value, which is described below. (c) Series of binary images of the image in panel a with the α value employed in the thresholding. From this example it can be seen that α values of 1.1 and 1.4 produced useful binary images where the cells are visible. (d) Cell counts per cm^2 as a function of α. Left: a line plot for 18 samples of NP, μP, and mP. Right: the mean and standard error of the mean plot for the 18 samples. The maximum peak is shown at $\alpha = 1.3$. Note that, when creating cell counts, a mimimum filter of 1 μm^2 and a maximum filter of 26 μm^2 were applied to remove false positives from protein debris and aggregated nuclei, respectively. (e) Higher-magnification DAPI image of the quantification process of a mP sample. (f) Intensities scanned along a horizontal (line 1) and vertical line (line 2). Note that the individual nucleus stained by DAPI can be differentiated in (e) image and (f) intensity peak.

humidified air. Cell culture reagents were purchased from a vendor (Thermo Fisher Scientific, Waltham, MA, USA) unless otherwise mentioned. During the cell seeding for each test, a small volume of growth media (200 μL) containing cells was applied to ensure the initial cell stabilization on top of each scaffold, and then media was added to cover the whole sample.

2.3.2. Cell Staining and Microscopy. After each test, the cultured cells were fixed with 4% paraformaldehyde for 30 min at room

temperature and permeabilized with 0.5% Triton X-100 (as a detergent). The samples were then washed three times using a Dulbecco's phosphate-buffered saline (DPBS) for 5 min each followed by two rinses with cold DPBS. Then, 1% bovine serum albumin (BSA) solution was applied to block nonspecific protein-binding sites. The filamentous-actin (F-actin) and nuclei were immuno-stained with two fluorescent dyes: Alexa Fluor 488 phalloidin (495/518 nm of excitation/emission wavelength) and DAPI (4′,6-diamidino-2-phenyl-indole, Vector Laboratories, 358/461 nm) for the F-actin and nuclei, respectively. Cell images on the substrate surface were acquired with a wide-field fluorescent microscope (BZ-X700, Keyence, Itasca, IL, USA). Surface morphology of the substrate was observed by bright field microscopy with oblique illumination. To acquire an image containing the whole substrate, 80 images were acquired and stitched semiautomatically (Figure 4a) through the software provided by the manufacturer.

2.3.3. Quantifying Cell Counts by Image Processing. Cell density was quantified from DAPI images using an image processing program coded with Matlab 2017a (Mathworks, Natick, MA, USA). In general, these image processing approaches have two major challenges: (1) representing the entire sample using only a partial image and (2) applying a single threshold for image binarization, which is determined without heuristic judgment, across a variety of images that have different relative brightness. It is common to have control images that have a different brightness than an experimental group, especially when performing extensive studies and/or employing large substrates (as is the case here). To resolve the first issue, 80 images (10 sets of 8 images) were stitched together cover the entire sample (Figure 4a and later in Figure 10a). To resolve the second issue, a new method, hereforward referred to as the histogram-based threshold algorithm (HTA), was developed to avoid subjective judgment when determining a threshold value, here referred to as α. In this method, a relative threshold replaces an absolute one in the HTA and is determined by using the number of the cells as an index. The general principal of the HTA is described in Figure 4b−d and a detailed description is provided in the Supporting Information. The image intensity of the substrate without cells (8 000−10 000, arbitrary unit) and macropores without cells (no substrate, 8 000−10 000) are low, as compared to the cell nuclei (over 15,000), which demonstrates that the DAPI signal from the substrate due to autofluorescence is negligible. After the thresholding, a minimal size filter (1 μm^2) was applied to remove protein fragments and a maximum size filter (26 μm^2) was used to exclude aggregated nuclei. A threshold is applied, similar to those used in open source programs such as ImageJ. However, the determination of the threshold value is unique to the HTA, which allows it to avoid the subjective nature of user defined threshold values, which can add undue variability and error to experimental measurements. The Otsu's method[29] is widely used for the automatic thresholding but the method is not effective for the large, high-resolution, and stitched images, such as those in our study. Thus, this method is proposed to be an objective and rational way to set a threshold from a statistical histogram of intensity profiles.

2.3.4. Adhesion Test. MG63 cells were seeded onto the three types of specimens at cell densities of 4 × 10^5 cells/well in a 12-well culture dish (Nest Biotech Co., Rahway, NJ, USA). Once cells were attached samples were moved to another well to exclude any cells that may have attached to the culture dish from the analysis. Samples were fixed and immunostained after 4 and 8 h of cell seeding, employing the procedures described above in Section 2.3.2. (Cell staining and microscopy). Once stained, samples were observed by optical microscopy and the number of attached cells were identified on the surface of the scaffold samples using the HTA image analysis method. The adhesion test and the corresponding image analyses were performed on three samples (N = 3) for each condition. To confirm the effect of the pores on scaffolds, a specific cell number (the number of initially attached cells divided by the surface area) was evaluated. The material density of individual scaffold samples for the adhesion test was calculated from the measured the bulk volume (the cross-sectional area multiplied by the height) and the measured weight of

each sample. The area of macroporous voids was subtracted from the bulk volume.

2.3.5. Proliferation Test. A proliferation assay was performed using a cell counting kit-8 (CCK-8, Sigma-Aldrich, St. Louis, MO, USA) based on WST-8 (2-(2-methoxy-4-nitrophenyl)-3-(4-nitrophenyl)-5-(2,4-disulfophenyl)-2H-tetrazolium, monosodium salt), which yields a water-soluble formazan dye by reduction in the presence of an electron carrier, 1-methoxy-5-methylphenazinium methylsulfate.[30] WST-8 is reduced by cellular dehydrogenases to an orange formazan product that is soluble in tissue culture medium and the amount of formazan produced is directly proportional to the number of living cells.[31]

To validate the number of cells in the whole volume of the 3D scaffold we obtain a standard curve of cell proliferation as a control group. Various densities of the cells were seeded on each well: 0.05, 0.1, 0.2, 0.4, 0.8, and 1.6 × 10^5 cells/well. For the test samples, an excessive number of cells (because of the leakage of cells to the polystyrene dish well) were seeded at cell densities of 2 × 10^5 cells/well in the 12-well culture dish for 3 and 5 days. The samples were moved to another well to exclude the cells attached to the polystyrene culture dish before performing the proliferation test. A 1:9 volume ratio of CCK-8 solution to DMEM was mixed and added to each well and incubated for 2 h in a cell incubator. After 2 h, the media on each well were slightly agitated on the well, and then placed in a 96-well plate. The absorbance (optical density, O.D.) at a 450 nm wavelength with a reference O.D. at a 600 nm wavelength were obtained, the O.D. at 450 nm was subtracted from the O.D. at 600 nm to remove the background intensity. Then, the values were converted to the cell numbers using the standard curve determined by a control group on the polystyrene culture dishes with different cell densities (0.05−1.6 × 10^5 cells). After each test, the cells were rinsed twice with DPBS and fixed. The proliferation test was performed on three samples (N = 3) for each condition.

2.3.6. Differentiation Test. Cell differentiation was investigated by measuring alkaline phosphatase (ALP) activity on day 7 and 14. The degree of cell differentiation measured by the ALP activity was quantified as an early stage indicator of the osteoblastic cell differentiation using p-nitrophenyl phosphate (p-NPP, Abcam, Cambridge, MA, USA). When employed, p-nitrophenol (p-NP), which is converted from p-NPP and is induced by ALP activity results in a color change, which, when analyzed using a plotted standard curve, can be converted to the ALP activity.[32] After 7 and 14 days of cell culture, the cells on each scaffold were lysed using a provided ALP assay buffer and collected in vials. The cell lysates (the products of the lysis of cells) on each well were slightly agitated and then reacted with a p-NPP solution. After 1 h, the solution turned yellow in color due to the ALP activity. The solutions on each vial were slightly agitated and then placed in a 96-well plate. The O.D. at 405 nm was obtained as following the manufacturer's instruction. The ALP activity test was performed on three samples (N = 3) for each condition.

2.3.7. Microcomputed Tomography of Cell Distribution on the 3D Scaffold. The cells and scaffolds were fixed with 2.5% glutaraldehyde/2% formaldehyde in 0.15 M cacodylate buffer for 24 h. After fixation, the samples were washed with DPBS and then placed into 2% osmium tetroxide (OsO₄)/1.5% potassium ferrocyanide in 0.15 M cacodylate buffer containing 2 mM CaCl₂. High-resolution X-ray microcomputed tomography (μ-CT, Xradia 510 Versa, Zeiss, Pleasanton, CA) was used for imaging cell distributions in a three-dimensional volume of interest with a 7.083 μm voxel size at a 40 kV acceleration voltage as well as a 0.779 μm voxel size at a 60 kV acceleration voltage. The rotation angle and tilt increment were 360° and 0.2°, respectively. The images and three-dimensional reconstructed models were developed using Amira software (FEI Visualization Sciences Group, Burlington, MA). OsO₄ was employed as it is capable of staining adherent human cells (e.g., HeLa) and some intracellular structure, while not staining the mineralized structures.[33,34] Because we used glutaraldehyde as a fixative, the cells can be stained enough to show heavy metal elements in their intracellular matrices and be visualized in μ-CT. In addition, micrographs were obtained by an optical microscope (VHX1000, Keyence, Osaka, Japan) to support the distribution of the OsO₄-stained MG63 cells
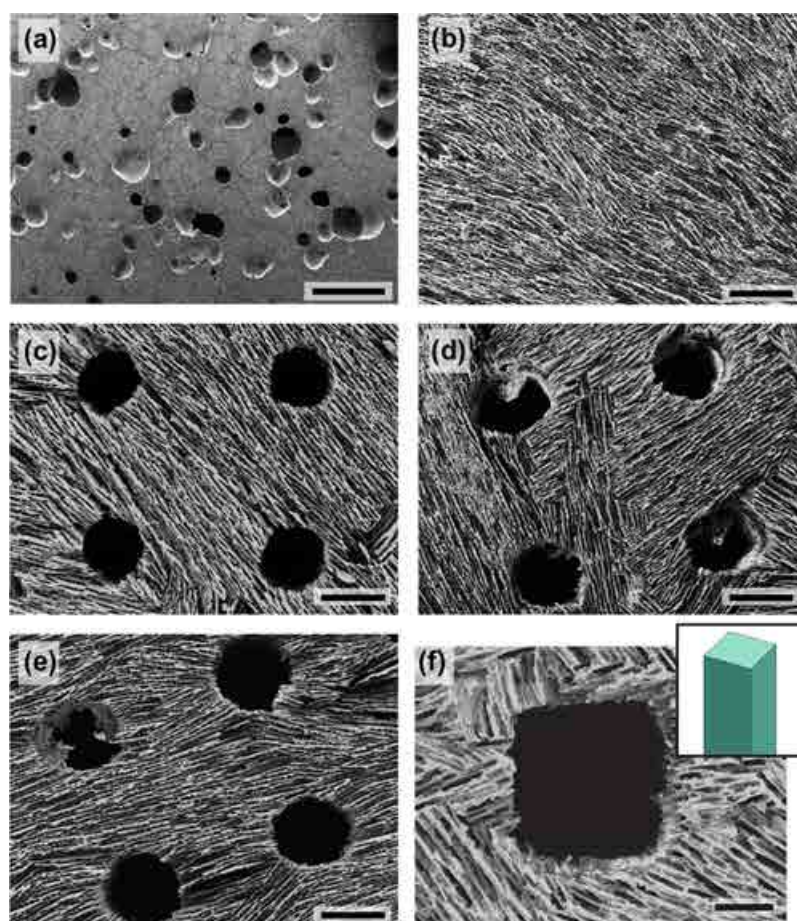
Figure 5. Cross-sectional micrographs of freeze-cast scaffolds: templated with round pins. Control samples with (a) no pores and (b) no template but micropores; and templated with round pins with diameters of (c) 600, (d) 700, and (e) 800 μm. Scale bars: 500 μm. (f) An alternative, square macropore shape. The inset shows the cross-sections of the solid model of the square pins that were used in this case. Scale bar: 200 μm.

along the transverse- and longitudinal cross sections. No staining of the HA substrates was observed.

2.3.8. Statistical Analysis. Statistical analysis was performed using a Student's *t* test for two groups and a one-way ANOVA and subsequent multicomparison tests (HST) for multiple groups, respectively.[35]

3. RESULTS AND DISCUSSION

3.1. Materials Characterization. Micrographs of the templated freeze-cast microstructures are shown in Figure 5. There are clear differences between the larger macro-porosity, created by the 3D printed template, and the small micro-porosity, created by the growth of ice crystals (as shown in Figure 3c). Measurements of both micro- and macropores are shown in Table 1. Measurements for the nonporous samples are shown in Figure 5a; the general morphology of the surface is similar to other reports of the sintered HAs with 2 wt % PVA[36] (irregularly sized, circular macropores up to 500 μm in diameter) and no PVA[37] (without circular macropores), while our NP sample (1 wt % PVA) show smaller closed macropores (less than ∼200 μm in diameter without interconnection between the pores, see Figure 5a). For the NP samples prepared by conventional methods, controlling the size and shape of macropores is challenging as they are influenced by many variables, such as the sintering temperature, holding time at maximum sintering temperature, composition of PVA, and irregular internal thermal conduction rate due to the complex size and shape, as described in the previous

reports.[37,38] However, the microporosity produces similar values regardless of the presence or size of the template, in all cases producing pores of $A_p \approx 2200$ μm^2 and $X_p \approx 6$. These values are comparable to previous reports on freeze-casting with HA solid loading and a water freezing agent.[16,39] The lower relative densities of macro- and microporous samples (calculated as fraction of materials for each sample multiplies the bulk density of HA, 2.6 g/cm^3,[40] shown in Table 1) imply that a lower manufacturing cost can be achieved in micro- (54%) and macro-porous (48% for 600 μm, 46% for 700 μm, and 39% for 800 μm) samples, compared to the bulk nonporous HA samples (assumed fully packed with 100% of fraction).

Given that the fabrication of the macro-porosity in this technique is driven by the use of 3D printed templates, the shape is not limited to a circular cross-section. As proof of this concept, an alternative, square macroporosity template was prepared (Figure 5f). The only change to the process was to design and print a templating array (as shown in Figure 2) that features pins of a square cross-sectional shape. As with the circular macropores, there is some warping to the original shape in each case. However, this level of control could provide an attractive method of creating microstructures with porosity tailored to specific experimental requirements.

Dimensions of the macroporosity are plotted in Figure 6. In most cases, the circular cross-section has been slightly distorted into an ellipse resulting in values of $X_p = 1.14–1.20$. This is most likely the result of the sintering process where the
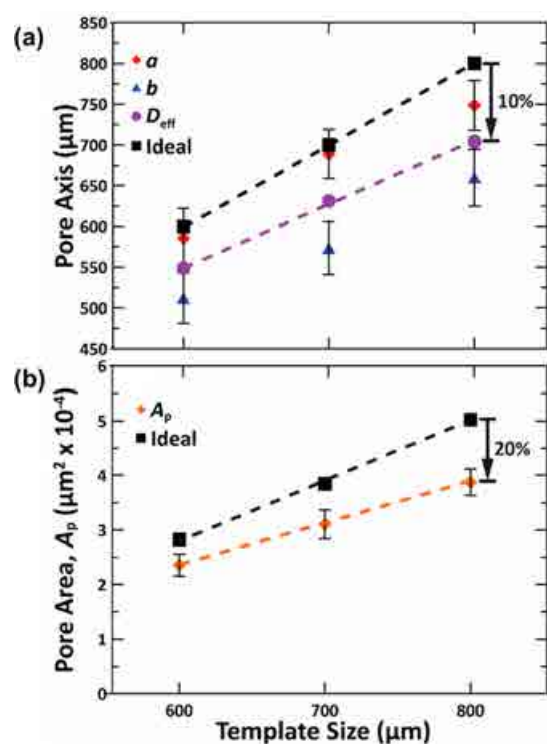
Figure 6. Dimension measurements after sintering process to remove the polymer templates. (a) Pore axis changes with respect to the template sizes. (b) Pore area changes with respect to the template sizes. *a*, the elliptic major axis (red diamond symbol); *b*, minor axis (blue triangle symbol); D_{eff}, a characteristic dimension (calculated as $D_{eff} = (a + b)/2$, purple circular symbol); and A_p: pore area ($ab\pi/4$, orange diamond symbol). A black square symbol shows the initial pin size of 3D printed templates.

templating pin was incinerated. Given this distortion, an effective diameter, D_{eff}, was calculated as $D_{eff} = (a + b)/2$ to make comparisons between the initial template and the final macro-porosity. The results are listed in Table 1 and plotted along with the measured values of a and b in Figure 6a. When comparing this to the ideal pore (i.e., with the exact diameter of the initial 3D printed templated pins), the final macro-porosity D_{eff} is only reduced by ~10% in all cases. Similarly, A_p only experiences a reduction of ~20% compared to the ideal pore size (Figure 6b). As a result, this method is capable of consistently providing pores similar in size and shape to the initial template.

In addition to controlling the macroporosity size within the final scaffold, the use of a 3D printed template allows for interpenetration between microporosity and macroporosity within the final scaffolds (Figure 7). The low thermal conductivity of the template (~0.15 W/m K) combined with the lack of contact between the template and the coldfinger (as seen in Figure 3b) are proposed to result in a negligible temperature gradient between the solidifying slurry and the template during the freeze-casting process. As a result, ice crystals do not nucleate from the template itself and all ice growth within the slurry is maintained in a single direction, progressing from the coldfinger to the top of the slurry. It has previously been shown for freeze cast scaffolds that the nucleation point of ice within the slurry results in a denser material that transitions to a more porous and lamellar structure.[10,41] No such gradient in porosity is observed near the macropores in any of the current scaffolds (as is shown in
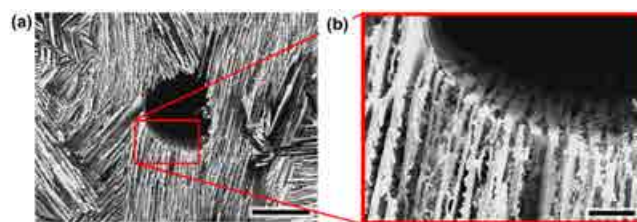
Figure 7. Scanning electron micrographs of the cross sections of macro-microporous scaffolds: (a) Interface between the macro- and microporosity; (b) When observing the interior wall at increased magnification, it can be seen that the microporosity runs directly into the macroporosity, creating interpenetration. Scale bars: (a) 500 and (b) 100 μm.

Figure 5). At the interface between micro- and macroporosity, the microporosity runs directly into the macroporosity, resulting in a continuous system of porosity at multiple length scales (Figure 7a, b). This could be beneficial for infiltration of fluids within these scaffolds to be used as chemical catalysts or water filters. However, for medical applications, which require a strict product quality assurance, reproducibility of the freeze casting scaffolds has to be further improved as introduced by Naleway et al. using ZrO_2-based ceramic scaffolds.[26] In addition, there have been reports that the HA may form second and/or third phases of calcium phosphate compounds (e.g., tricalcium phosphate, TCP) in addition to the pure HA phase when sintered over 1673 K (1400 °C);[42] however, HA scaffolds sintered between 1523 K and 1623 K (1250 to 1350 °C) did not typically yield the TCP phase when analyzed using XRD.[16,38,39] As same as the above references, only the pure HA phase was found from the ground powders of an mP sample, without other phases, in our XRD analysis (Figure S1). In summary, the structure of the bioinspired freeze cast was comparable to that of natural cortical bone (bovine femur), allowing for the bioinspired scaffold to mimic both the larger osteons and smaller lacuna spaces of natural bone, as shown in Figure 8.

3.2. Adhesion Assay. Adhesion assays were performed to examine the morphology of the cells on each HA substrate. Cells were immunostained with Phalloidin and DAPI at 4 and 8 h and observed under light microscopy. Morphologies of cells on NP, μP, and mP substrates are displayed in Figure 9: F-actin
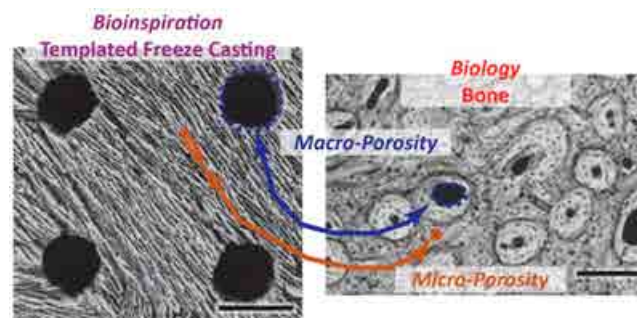
Figure 8. Comparison of the structure between the current, bioinspired freeze cast structures and that of natural cortical bone (bovine femur). In both cases, porosity is observed at multiple length scales allowing for the bioinspired scaffold to mimic both the larger osteons and smaller lacuna spaces of natural bone. Scale bars, bioinspiration; 500 μm; biology, 300 μm. The right image adapted with permission from ref 20. Copyright 2009 Elsevier.
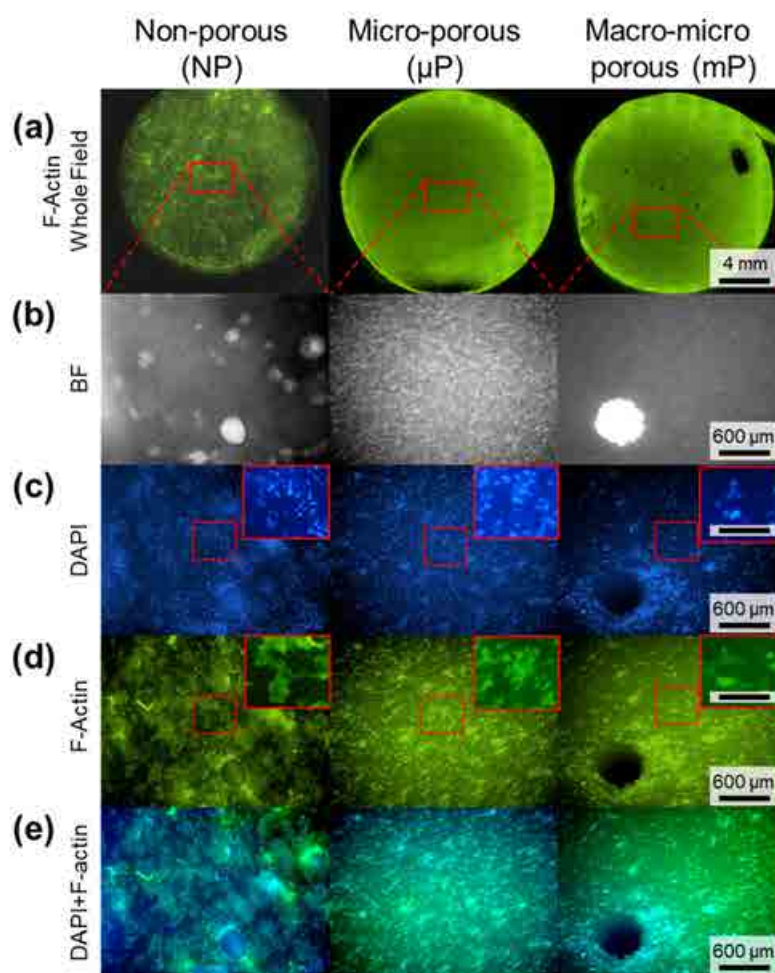
Figure 9. Optical microscopy micrographs of the adhesion assay results. (a) F-actin image of the whole substrate. Scale bar = 4 mm. 80 planes (10 sets of 8 images) of 4× images are stitched together (a total of 5670 × 5272 pixels in the image, 960 × 720 pixels/image). (b) Bright-field (BF) images showing the surface characteristic of HA. (c) DAPI images showing cell nuclei. (d) Phalloidin images showing actin stress fibers (F-actin). Cells are a polygonal shape in NP but demonstrate an elongated morphology along micropores on the μP and mP substrates. (e) DAPI+DPI images. Scale bar for insets of b−e = 200 μm.

images of a whole substrate are shown in Figure 9a, the substrate surfaces shown in Figure 9b, nuclei in Figure 9c, e, and the actin stress fibers in Figure 9a, d, e. Micropores with an elliptical shape are observed on μP and mP substrates but not in NP (Figure 9b). This is due to the smoother surface of the NP when compared to the μP and mP. Note that the dimple-like shapes on the NP surface are residual craters, as previously described, which were not removed during the surface treatment. A macropore with a diameter of ∼550 μm is seen at the lower left corner of the mP substrate. F-actin images of a whole substrate exhibit an even distribution of cell seeding (Figure 9a). Morphologies of actin (Figure 9a, d), nuclei (Figure 9c) and actin-nuclei mergence (Figure 9d) prove good biocompatibility between the cells and the HA substrate. Interestingly, mP has a higher cell density around the macropore. Although it is not currently clear what causes this, two possibilities are proposed: first, the cells are trapped around the macro-pore when media flows through it or, second, cells are migrating to the macro-pore after seeding. The cell shape is affected by the presence of micropores. In the absence of micropores in the NP sample, cells display polygonal shapes and have no specific orientation. In contrast, both samples with micropores (μP and mP) display an elongated shape of cells

which are oriented parallel to the direction of the micropore grooves (Figure 9d, e).

The cell seeding density can be impacted by the physical/chemical properties of the substrate (e.g., hydrophobicity) as cell culture vessels are treated to improve or inhibit adhesion to cells.[43,44] Structural properties can also impact the cell seeding results. The macropores in the mP samples, in particular, would negatively work as a drain that washes cells away from the scaffold and decreases the cell density in the seeding procedure. To confirm how these factors affected the cell distribution and growth on these scaffolds, the cell density was examined and compared between the three different samples. After both 4h and 8h of cell attachment (Figure 10a), cell densities showed no statistically significant differences between NP, μP, and mP, hence indicating that the cell seeding was evenly distributed. To analyze the number of cells, we applied and compared two methods: one was to apply the HTA with a fixed multiplier (i.e., α = 1.3 from the mean of all samples), and another was to apply the HTA with an iterative multiplier value (i.e., a different α for each sample). Both methods with fixed and iterative multiplier lead to similar results (Figure 10a). The number of cells on the μP samples are statistically higher than the NP samples after 4 h of cell seeding, but there is no statistically significant difference
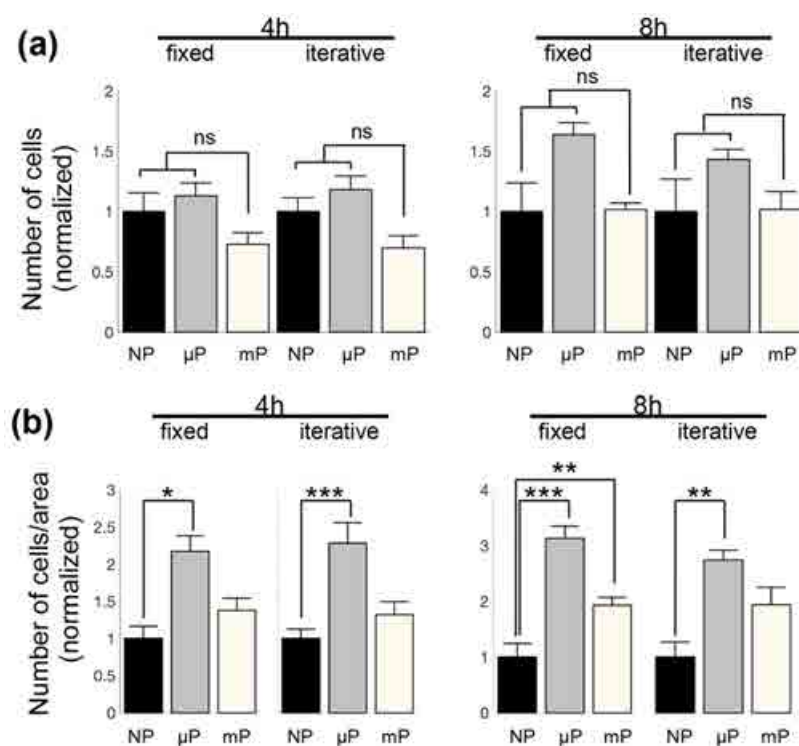
Figure 10. Adhesion assay results normalized by the number of cells on the NP samples as 1 at each time. (a) Number of cells at 4 and 8 h. (b) Number of cells per area at 4 and 8 h. The number of cells is measured by image processing using a histogram-based threshold algorithm (HTA). Note that "fixed" means that the multiplier value (α) is set to 1.3, whereas "iterative" means that α is chosen for each individual measurement and is set at the threshold where the maximum number of cells are apparent. Please see Appendix for details. $N = 3$ for each bar. Note that $*$ $p < 0.05$, $**$ $p < 0.01$, $***$ $p < 0.001$, and "ns" means not statistically significant.
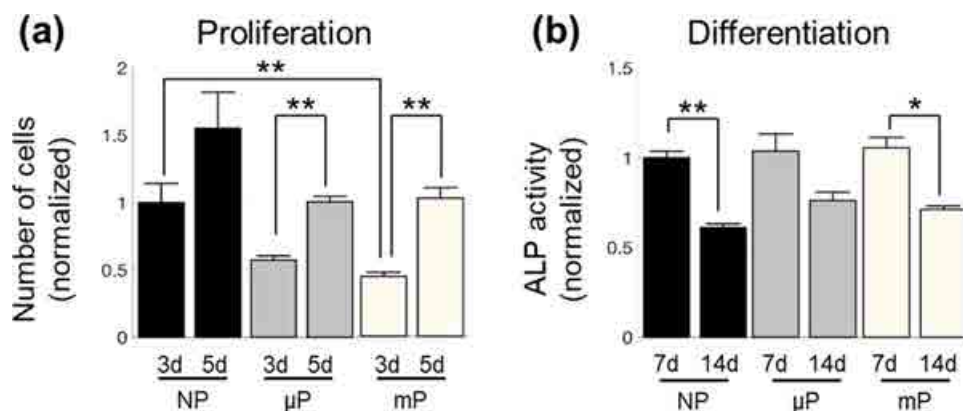
Figure 11. (a) Proliferation results on days 3 and 5. The number of cells is obtained by a cell counting kit (CCK) and a microplate reader. Data are normalized by the value of NP on day 3. (b) Differentiation results on days 7 and 14. ALP activity is measured. Data are normalized by the value of NP on day 7. $*$ $p < 0.05$, $**$ $p < 0.01$, statistical test were performed by one way ANOVA and subsequent multicomparison tests (HST). $N = 3$ was used for each bar. Error bars are presented as the standard error of the mean.

between the NP and mP samples ([Figure 10](#)b). After 8 h, the differences among these three samples are more distinct: the μP showed the highest value, implying that this is the most efficient structure to hold as many cells as possible. Because of the lowest density of the mP samples, it was expected to have the highest value when considering the amount of materials used; however, the mP samples showed the lower value than the μP samples possibly due to the fact that it has either (1) a lower surface area for cell attachment than the μP samples or (2) a drain effect of cells during the cell seeding process. Because of the limitation of in vitro test, which is not able to fully replicate the effect of macropores in an in vivo test, further investigations are needed

to confirm the possible reason for the lower value of mP samples than μP samples. For example, the macropores may be able to induce angiogenesis and bone ingrowth, however these types of results would only be possible to determine with an in vivo test. Calculation of the surface area in 3D and in vivo comparative measurements of cell attachment of each sample are outside the scope of this current work but may be a future direction of this research.

In summary, adhesion tests revealed good biocompatibility, uniform cell seeding, and different cell morphologies based on the substrate type (NP, polygon; vs μP/mP, elongation parallel to the HA wall direction). In addition, considering the material
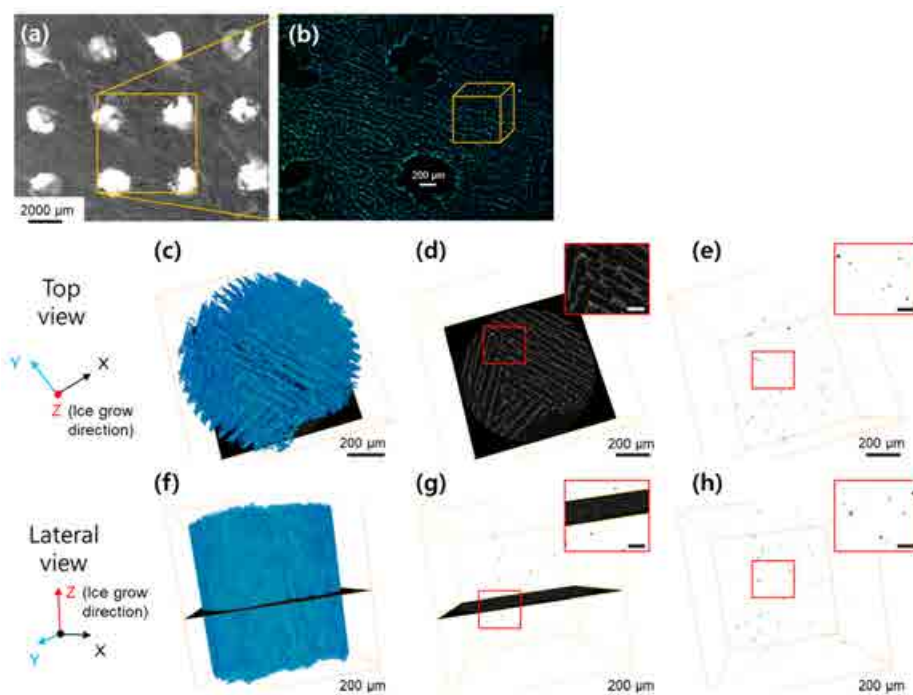
Figure 12. Cell distribution of the macro−microporous scaffold. (a) Optical micrograph. (b) Fluorescent microscopy image stained with DAPI (blue, cell nucleus) and β-actin (green, actin filament) dyes. Top views of the 3D rendered cells (stained with OsO_4) in the macro−microporous scaffold displayed with (c) the HA lamella wall structure (blue), (d) an orthoslice image (gray scale) of the scaffold with the stained cells (red dots), and (e) only the cells (red dots). Lateral views of 3D rendered cell (stained with OsO_4) in the macro−microporous scaffold are displayed with (f) the HA lamella wall structure (blue), (g) an orthoslice image (gray scale) of the scaffold with the stained cells (red dots), and (h) only cells (red dots). Insets of d, e and g, h are magnified images of each red rectangle region. Scale bars of insets: 100 μm.

processing and cost, a higher efficiency of material usage can be achieved in the μP and mP samples, and thus the process cost can be reduced while maintaining the high osteoconductive properties required for tissue engineering scaffolds.

3.3. Proliferation and Differentiation. The morphological gap described above in the adhesion assay section implies that cells have a discrepancy in cell functions. Thus, we have investigated proliferation and differentiation of the cells.

A proliferation assay was performed on days 3 and 5 using a CCK-8 method. Three days after seeding, NP has the highest cell number while μP and mP have lower cell numbers (57 and 47% of NP, respectively). These cell numbers increase and result in 65% and 66% of NP, respectively, by day 5. Regarding the increased number of cells among each sample, the μP and mP showed higher cell growth rates (160 and 210% after 2 days, respectively) than the NP samples (150%). These results exhibit that μP and mP induce MG63s into higher cell growth rate than P (Figure 11a), implying that the number of cells of μP and mP on day 7 or, potentially on a longer time frame, will be higher than NP; however this requires further investigations given that different phases of cell growth will occur.[45]

Cell differentiation was investigated by measuring ALP activity on day 7 and 14 as shown in Figure 11b. On day 7, there were no differences in ALP activities among the three samples, while, on day 14, activities are decreased by 61, 73, and 67% in NP, μP, and mP, respectively. The amount of activity decrease is the largest in NP, however no statistically significant differences ($p < 0.05$) were observed between μP or mP (Figure 11b).

In conclusion, the highest cell proliferation is shown in NP, but a higher cell growth rate is observed in μP and mP. There are no significant differences in differentiation among three

substrates. Similar to the NP samples, the μP and mP samples showed slightly less but similar level of proliferation and differentiation, indicating that the freeze-casting and sintering process of the 3D templated polymer are biocompatible without any harmful residues on the samples. This serves as a promising direction for forming biocompatible, as well as customizable, biomedical materials.

3.4. μ-CT of Cell Distribution on the 3D Scaffolds. Using a high resolution μ-CT scan allows for the HA scaffold and the OsO_4-stained cells to be differentiated,[46,47] which along with the low- (bright field, stitched in Figure 12a) and high-resolution (immunofluorescent with DAPI and F-actin in Figure 12b) images showed the cells seeded across the surface and aligning in-plane with the lamellar walls (Figure 12c). Furthermore, cells were found throughout the depth of the scaffold (Figure 12d, e, along the Z-axis). Lateral images of μ-CT also showed a homogeneous distribution of cells along the ice growth direction (the Z-axis in Figure 12f−h). To ascertain the cell distribution similar to the previous research,[46,47] optical micrographs along the transverse- and longitudinal- cross sections were obtained to show the cell distribution from a different modality from the X-ray (Figure S2). Please note that the HA substrates were not stained by OsO_4 solutions, which specifically stained the MG63 cells only. This penetration of cells may be related to the effect of the macro-porosity, allowing the cells to travel deep within the scaffold through extracellular fluids before adhering to the scaffold walls. This result suggests the conclusion that osteocytes, found in the lacunae spaces, would be able to migrate through the macropores and adhere within the micropores where they would promote the exchange of nutrients and accelerate the bone regeneration process.

4. CONCLUSIONS

To mimic the multiscale hierarchical structure of natural compact bones, a combination of the freeze-casting process and 3D printing was applied to produce porosity at multiple length scales. These scaffolds were evaluated for their cellular activities and biocompatibility using an osteoblast-like MG63 cell line, resulting in the following conclusions:

- The size and shape of pores were easily controlled by the size and shape of the user-defined 3D printed templates: three different pore sizes (600, 700, 800 μm) and two different shapes (circular and square shape) were realized.
- The 3D printed templating method was capable of producing pores similar in size to the initial template, reducing by only 10% of the ideal effective diameter (D_{eff}) and 20% of pore areas (A_p).
- Adhesion test results of osteoblast-like MG63 cell lines on the three substrates show that the morphology of the cells were affected by the substrates. On the nonporous samples, the cells showed a polygonal shape with no orientation, whereas the cells on the microporous and macro−microporous samples were elongated parallel to the direction of micropore grooves. In addition, a higher density of cells was observed around macropores from the edge of pores, implying cell migration and/or a drainage effect during the cell seeding.
- Initial attachment of MG63 cells were maintained at a similar level while reducing the amount of material used by implementing both the micro- and macropores into the substrate.
- A newly developed histogram-based threshold algorithm was effective in evaluating the number of cells on the entire surface of the substrate, improving on previous methodologies that may result in additional error or variability.
- The cell growth rate was higher in micro- and macro-micro porous samples than nonporous samples, and more importantly, no significant toxicity was found in any of the micro- or macro-micro porous samples or nonporous samples, indicating that there was no residual toxin in the scaffolds.
- 3D high-resolution micro-computed tomography micrographs show that the cells were able to be distributed throughout the macro-micro porous scaffold, penetrating deep into the core of the scaffold.

5. LIMITATIONS AND FUTURE WORK

We do not have sufficient data on the structural integrity of these scaffolds to test mechanical properties. In future work, we will look to infiltrate polymer through the pore spaces to strengthen the scaffold.

■ ASSOCIATED CONTENT

Ⓢ Supporting Information

The Supporting Information is available free of charge on the ACS Publications website at DOI: 10.1021/acsbiomaterials.8b01308.

> Histogram-based threshold algorithm, XRD diffraction pattern of the HA scaffold, and optical micrographs of mP sample along transverse- and longitudinal cross-section (PDF)

■ AUTHOR INFORMATION

Corresponding Author

*E-mail: shur@ucsd.edu. Phone: +1-858-534-5086. Fax: +1-858-822-1160. Address: 9500 Gilman Drive, SERF BLDG #259A, La Jolla, CA 92093-0435, USA.

ORCID Ⓞ

Sung Sik Hur: 0000-0003-4211-0497

Author Contributions

†J.-Y.J. and S.E.N. contributed equally.

Notes

The authors declare no competing financial interest.

■ ACKNOWLEDGMENTS

■ REFERENCES

(1) Meyers, M. A.; McKittrick, J.; Chen, P.-Y. Structural biological materials: Critical mechanics-materials connections. *Science* **2013**, *339*, 773−779.

(2) Arzt, E. Biological and artificial attachment devices: Lessons for materials scientists from flies and geckos. *Mater. Sci. Eng., C* **2006**, *26* (8), 1245−1250.

(3) Naleway, S. E.; Porter, M. M.; McKittrick, J.; Meyers, M. A. Structural Design Elements in Biological Materials: Application to Bioinspiration Structural Design Elements in Biological Materials: Application to Bioinspiration. *Adv. Mater.* **2015**, *27* (37), 5455−5476.

(4) Weaver, J. C.; Milliron, G. W.; Miserez, A.; Evans-Lutterodt, K.; Herrera, S.; Gallana, I.; Mershon, W. J.; Swanson, B.; Zavattieri, P.; DiMasi, E.; Kisailus, D. The stomatopod dactyl club: A formidable damage-tolerant biological hammer. *Science* **2012**, *336* (6086), 1275−1280.

(5) Meyers, M. A.; Lin, A. Y. M.; Chen, P.-Y.; Muyco, J. Mechanical strength of abalone nacre: Role of the soft organic layer. *Journal of the Mechanical Behavior of Biomedical Materials* **2008**, *1* (1), 76−85.

(6) Menig, R.; Meyers, M. H.; Meyers, M. A.; Vecchio, K. S. Quasi-static and dynamic mechanical response of Haliotis rufescens (abalone) shells. *Acta Mater.* **2000**, *48* (9), 2383−2393.

(7) Naleway, S. E.; Taylor, J. R. A.; Porter, M. M.; Meyers, M. A.; McKittrick, J. Structure and mechanical properties of selected protective systems in marine organisms. *Mater. Sci. Eng., C* **2016**, *59*, 1143−1167.

(8) Munch, E.; Launey, M. E.; Alsem, D. H.; Saiz, E.; Tomsia, A. P.; Ritchie, R. O. Tough, bio-inspired hybrid materials. *Science* **2008**, *322*, 1516−1520.

(9) Deville, S.; Saiz, E.; Nalla, R. K.; Tomsia, A. P. Freezing as a path to build complex composites. *Science* **2006**, *311*, 515−518.

(10) Deville, S.; Saiz, E.; Tomsia, A. P. Ice-templated porous alumina structures. *Acta Mater.* **2007**, *55*, 1965−1974.

(11) Deville, S. Ice-templating, freeze casting: Beyond materials processing. *J. Mater. Res.* **2013**, *28* (17), 2202−2219.

(12) Bai, H.; Wang, D.; Delattre, B.; Gao, W. W.; De Coninck, J.; Li, S.; Tomsia, A. P. Biomimetic gradient scaffold from ice-templating for self-seeding of cells with capillary effect. *Acta Biomater.* **2015**, *20*, 113−119.

(13) Jung, H.-D.; Yook, S.-W.; Kim, H.-E.; Koh, Y.-H. Fabrication of titanium scaffolds with porosity and pore size gradients by sequential freeze casting. *Mater. Lett.* **2009**, *63*, 1545−1547.

(14) Koh, Y.-H.; Jun, I.-K.; Sun, J.-J.; Kim, H.-E. In situ fabrication of a dense/porous bi-layered ceramic composite using freeze casting of a ceramic−camphene slurry. *J. Am. Ceram. Soc.* **2006**, *89* (2), 763−766.

(15) Li, W.; Porter, M. M.; Olevsky, E. A.; German, R. M.; McKittrick, J. Sintering of bi-porous titanium dioxide scaffolds: Experimentation, modeling and simulation. *Mater. Sci. Eng., A* **2015**, *636*, 148−156.

(16) Deville, S.; Saiz, E.; Tomsia, A. P. Freeze casting of hydroxyapatite scaffolds for bone tissue engineering. *Biomaterials* **2006**, *27*, 5480−5489.

(17) Porter, M. M.; McKittrick, J. It's tough to be strong: Advances in bioinspired structural ceramic-based materials. *Am. Ceram. Soc. Bull.* **2014**, *93* (5), 18−24.

(18) Lee, S.; Porter, M. M.; Wasko, S.; Lau, G.; Chen, P.-Y.; Novitskaya, E. E.; Tomsia, A. P.; Almutairi, A.; Meyers, M. A.; McKittrick, J., Potential bone replacement materials perpared by two methods. *MRS Online Proc. Libr.* **2012**, *1418*, DOI: 10.1557/opl.2012.671.

(19) Yoon, B.-H.; Koh, Y.-H.; Park, C.-S.; Kim, H.-E. Generation of large pore channels for bone tissue engineering using camphene-based freeze casting. *J. Am. Ceram. Soc.* **2007**, *90* (6), 1744−1752.

(20) Chen, P.-Y.; Stokes, A. G.; McKittrick, J. Comparison of the structure and mechanical properties of bovine femur bone and antler of the North American elk (Cervus elaphus canadensis). *Acta Biomater.* **2009**, *5* (2), 693−706.

(21) Rustom, L. E.; Boudou, T.; Lou, S.; Pignot-Paintrand, I.; Nemke, B. W.; Lu, Y.; Markel, M. D.; Picart, C.; Wagoner Johnson, A. J. Micropore-induced capillarity enhances bone distribution in vivo in biphasic calcium phosphate scaffolds. *Acta Biomater.* **2016**, *44*, 144−154.

(22) Porter, M. M.; Imperio, R.; Wen, M.; Meyers, M. A.; McKittrick, J. Bioinspired scaffolds with varying pore architectures and mechanical properties. *Adv. Funct. Mater.* **2014**, *24* (14), 1978−1987.

(23) Porter, M. M.; Yeh, M.; Strawson, J.; Goehring, T.; Lujan, S.; Siripasopsotorn, P.; Meyers, M. A.; McKittrick, J. Magnetic freeze casting inspred by nature. *Mater. Sci. Eng., A* **2012**, *556*, 741−750.

(24) Yaraghi, N. A.; Guarín-Zapata, N.; Grunenfelder, L. K.; Hintsala, E.; Bhowmick, S.; Hiller, J. M.; Betts, M.; Principe, E. L.; Jung, J.-Y.; Sheppard, L.; Wuhrer, R.; McKittrick, J.; Zavattieri, P. D.; Kisailus, D. A Sinusoidally Architected Helicoidal Biocomposite. *Adv. Mater.* **2016**, *28* (32), 6835−6844.

(25) Naleway, S. E.; Yu, C. F.; Porter, M. M.; Sengupta, A.; Iovine, P. M.; Meyers, M. A.; McKittrick, J. Bioinspired composites from freeze casting using clathrate hydrates. *Mater. Eng.* **2015**, *71*, 62−67.

(26) Naleway, S. E.; Fickas, K. C.; Meyers, M. A.; McKittrick, J. Reproducibility of ZrO$_2$-based freeze casting for biomaterials. *Mater. Sci. Eng., C* **2015**, *61*, 105−112.

(27) Naleway, S. E.; Yu, C. F.; Hsiong, R. L.; Sengupta, A.; Iovine, P. M.; Hildebrand, J. A.; Meyers, M. A.; McKittrick, J. Bioinspired intrinsic control of freeze cast composites: Harnessing hydrophobic hydration and clathrate hydrates. *Acta Mater.* **2016**, *114*, 67−79.

(28) Poinern, G. E. J.; Brundavanam, R. K.; Le, X.; Fawcett, D. The mechanical properties of a porous ceramic derived from a 30 nm sized particle based powder of hydroxyapatite for potential hard tissue engineering applications. *Am. J. Biomed. Eng.* **2012**, *2* (6), 278−286.

(29) Otsu, N. A Threshold Selection Method from Gray-Level Histograms. *IEEE Transactions on Systems, Man, and Cybernetics* **1979**, *9* (1), 62−66.

(30) Li, Q.; Yokoshi, M.; Okada, H.; Kawahara, Y. The cleavage pattern of TDP-43 determines its rate of clearance and cytotoxicit. *Nat. Commun.* **2015**, *6*, 6183.

(31) Ishiyama, M.; Tominaga, H.; Shiga, M.; Sasamoto, K.; Ohkura, Y.; Ueno, K. A Combined Assay of Cell Vability and in Vitro Cytotoxicity with a Highly Water-Soluble Tetrazolium Salt, Neutral Red and Crystal Violet. *Biol. Pharm. Bull.* **1996**, *19* (11), 1518−1520.

(32) Frohbergh, M. E.; Katsman, A.; Botta, G. P.; Lazarovici, P.; Schauer, C. L.; Wegst, U. G. K.; Lelkes, P. I. Electrospun hydroxyapatite-containing chitosan nanofibers crosslinked with genipin for bone tissue engineering. *Biomaterials* **2012**, *33* (36), 9167−9178.

(33) Barry, J. J. A.; Howard, D.; Shakesheff, K. M.; Howdle, S. M.; Alexander, M. R. Using a Core−Sheath Distribution of Surface Chemistry through 3D Tissue Engineering Scaffolds to Control Cell Ingress. *Adv. Mater.* **2006**, *18* (11), 1406−1410.

(34) Dorsey, S. M.; Lin-Gibson, S.; Simon, C. G. X-ray micro-computed tomography for the measurement of cell adhesionand proliferation in polymer scaffolds. *Biomaterials* **2009**, *30* (16), 2967−2974.

(35) Hochberg, Y.; Tamhane, A. C., Distribution-Free and Robust Procedures. In *Multiple Comparison Procedures*; John Wiley & Sons, Inc., 2008; pp 234−273. DOI: 10.1002/9780470316672.ch9

(36) Zuo, K. H.; Zeng, Y.-P.; Jiang, D. Effect of polyvinyl alcohol additive on the pore structure and morphology of the freeze-cast hydroxyapatite ceramics. *Mater. Sci. Eng., C* **2010**, *30*, 283−287.

(37) Hassan, M. N.; Mahmoud, M. M.; Link, G.; El-Fattah, A. A.; Kandil, S. Sintering of naturally derived hydroxyapatite using high frequency microwave processing. *J. Alloys Compd.* **2016**, *682*, 107−114.

(38) Zuo, K. H.; Zeng, Y.-P.; Jiang, D. Effect of polyvinyl alcohol additive on the pore structure and morphology of the freeze-cast hydroxyapatite ceramics. *Mater. Sci. Eng., C* **2010**, *30* (2), 283−287.

(39) Fu, Q.; Rahaman, M. N.; Dogan, F.; Bal, B. S. Freeze-cast hydroxyapatite scaffolds for bone tissue engineering applications. *Biomed. Mater.* **2008**, *3*, 025005.

(40) Poinern, G. E. J.; Brundavanam, R. K.; Le, X. T.; Fawcett, D. The mechanical properties of a porous ceramic derived from a 30 nm sized particle based powder of hydroxyapatite for potential hard tissue engineering applications. *Am. J. Biomed. Eng.* **2012**, *2* (6), 278−286.

(41) Xia, Z. M.; Yu, X. H.; Jiang, X.; Brody, H. D.; Rowe, D. W.; Wei, M. Fabrication and characterization of biomimetic collagen-apatite scaffolds with tunable structures for bone tissue engineering. *Acta Biomater.* **2013**, *9* (7), 7308−7319.

(42) Muralithran, G.; Ramesh, S. The effects of sintering temperature on the properties of hydroxyapatite. *Ceram. Int.* **2000**, *26* (2), 221−230.

(43) Ramsey, W. S.; Hertl, W.; Nowlan, E. D.; Binkowski, N. J. Surface treatments and cell attachment. *In Vitro* **1984**, *20* (10), 802−808.

(44) Shen, M.; Horbett, T. A. The effects of surface chemistry and adsorbed proteins on monocyte/macrophage adhesion to chemically modified polystyrene surfaces. *J. Biomed. Mater. Res.* **2001**, *57* (3), 336−345.

(45) Butler, M. *Animal Cell Culture and Technology*; Taylor & Francis, 2004.

(46) Hilldore, A.; Wojtowicz, A.; Johnson, A. W. Micro-CT based quantification of non-mineralized tissue on cultured hydroxyapatite scaffolds. *J. Biomed. Mater. Res., Part A* **2007**, *82A* (4), 1012−1021.

(47) Papantoniou, I.; Sonnaert, M.; Geris, L.; Luyten, F. P.; Schrooten, J.; Kerckhofs, G. Three-dimensional characterization of tissue-engineered constructs by contrast-enhanced nanofocus computed tomography. *Tissue Eng., Part C* **2014**, *20* (3), 177−187.